ELSEVIER

Contents lists available at ScienceDirect

Journal of Power Sources

journal homepage: www.elsevier.com/locate/jpowsour





In situ anodic electrodeposition of two-dimensional conductive metal-organic framework@nickel foam for high-performance flexible supercapacitor

Hongxing Jia^{a,1}, Shun Lu^{a,1}, Sun Hae Ra Shin^b, Maria L. Sushko^b, Xiaoping Tao^c, Matthew Hummel^a, Praveen K. Thallapally^{b,***}, Jun Liu^{b,**}, Zhengrong Gu^{a,*}

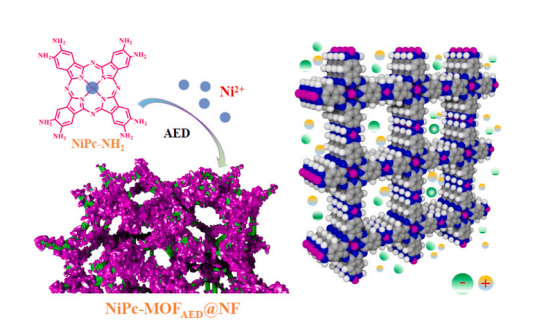
- ^a Department of Agricultural and Biosystems Engineering, South Dakota State University, Brookings, SD, 57007, USA
- ^b Physical and Computational Science Directorate, Pacific Northwest National Laboratory, Richland, WA, 99352, USA
- ^c Center for Energy & Environmental Science, Interdisciplinary Cluster for Cutting Edge Research, Shinshu University, 4-17-1 Wakasato, Nagano-shi, Nagano, 380-8553, Japan

HIGHLIGHTS

Anodic electrodeposition approach was first used to construct 2D conductive MOF.

- AED approach could effectively suppress aggregation of NiPc-MOF.
- AED approach is one-step approach without binders/conductive additives.
- NiPc-MOF_{AED}@NF supercapacitor demonstrate outstanding performance.

GRAPHICAL ABSTRACT



ARTICLE INFO

Keywords:
2D conductive metal-organic frameworks
In situ electrodeposition
Phthalocyanine
Supercapacitor

ABSTRACT

Owing to their large specific surface area and well-defined porosity, metal-organic frameworks (MOFs) have long been considered as promising materials for energy storage. Unfortunately, their straightforward utilization in supercapacitors was hindered for years due to poor conductivity until the emergence of 2D conductive MOF materials. To date, several 2D conductive MOF-based supercapacitors have been reported. Nevertheless, almost all these supercapacitors were fabricated from MOF powders through a slurry coating method or dense packing method, which negatively affected their capacitor performance. Herein, we have developed an anodic electrodeposition (AED) approach to fabricate a uniformly deposited 2D conducting MOF on nickel foam and use it directly as electrodes for supercapacitors without any additives. The superior performance of the 2D conducting MOF on nickel foam in both aqueous and organic electrolytes was then disclosed by a series of electrochemical measurements, demonstrating the significant advantages of the AED approach over traditional methods.

E-mail addresses: Praveen.Thallapally@pnnl.gov (P.K. Thallapally), jun.liu@pnnl.gov (J. Liu), zhengrong.gu@sdstate.edu (Z. Gu).

^{*} Corresponding author.

^{**} Corresponding author.

^{***} Corresponding author.

¹ These authors (H. Jia and S. Lu) contributed equally to this work.

1. Introduction

Metal-organic frameworks (MOFs) are a novel class of materials with remarkable features, including large specific surface area, mild reaction conditions, and well-defined porosity as well as controllable structures and functionalities, which make them promising candidates for many applications [1]. So far, a variety of MOFs have been synthesized and utilized in a wide range of applications, including but not limited to gas storage/separation [2,3], optical and magnetic materials [4,5], sensors [6], catalysis [7], and drug delivery [8]. Further, MOF materials have also been regarded as promising candidates for energy storage, yet their applications in supercapacitors have been severely limited due to their poor electrical conductivity [9]. To address this issue, scientists have developed various strategies which can be categorized into two classes. One strategy is introducing pyrolysis process [10,11]. Although MOF can be converted into conductive carbon materials, their chemical structures will be destroyed during pyrolysis. Another strategy is using conductive additives and binders such as graphene [12], polyaniline [13], polypyrrole [14] to construct conducting pathway. Nevertheless, the pores in MOFs will be blocked by the conductive additives and binders, which would hamper the diffusion of ions in MOFs. Therefore, it is still a great challenge to prepare MOF-based electrode materials with both effective porosity and decent electrical conductivity for supercapacitors.

Recently, two-dimensional (2D) conductive MOFs with improved intrinsic electrical conductivity have been synthesized [15] and employed as electrocatalysts [16,17], gas sensors [18], and so on, which presents a different way of addressing this issue. So far, several 2D conductive MOFs have been utilized for supercapacitors [9,19-22]. In these previous works, 2D conductive MOFs were usually synthesized initially as the powder/film through solvothermal approach, after which a transfer and/or reshaping process is necessary for the electrode fabrication. In most cases, the electrodes of 2D conductive MOFs were still prepared with conductive additives and binders through the slurry coating method. In doing so, their superior intrinsic conductivity over traditional MOFs was obscured. Moreover, the use of additives might reduce the effective surface area and negatively affect long-term cycling performance [23]. To avoid the use of additives, scientists also tried to press 2D conductive MOFs into self-supported pellets [9,20]. Unfortunately, due to dense packing under high pressure, many MOF particles inside pellets are not able to capture ions, leading to the decrease in capacitance [9]. Until now, restrained by flawed electrode fabrication approaches, the potential of 2D conductive MOFs in supercapacitors was still far from fully exploited.

The electrochemical deposition technique is a promising approach to fabricating 2D conductive MOFs as electrodes, with significant advantages over above methods [24]. On the one hand, electrochemical deposition allows *in situ* growth of 2D conductive MOFs on substrates, thus reducing the cost and simplifying the process. On the other hand, binders, conductive additives, and compacting processes are no longer necessary, which will help improve the capacitor performance. Moreover, the electrochemical deposition process could be conducted at mild conditions and all parameters could be precisely controlled, which makes it a mild, facile method with good reproducibility. To date, there is still no study to prepare 2D conductive MOFs through direct electrochemical deposition.

In 2018, we reported the first synthesis of a phthalocyanine-based 2D conductive MOF (NiPc-MOF) with a formula of $[\mathrm{Ni}_3(\mathrm{C}_{32}\mathrm{H}_{16}\mathrm{N}_{16})]_n$ and its outstanding performance toward water oxidation [25]. Owing to the high electrical conductivity ($\sim\!0.2~\mathrm{S~cm}^{-1}$) and large surface area ($\sim\!593~\mathrm{m}^2~\mathrm{g}^{-1}$), NiPc-MOF is also considered as a promising electrode material for supercapacitors. In this present report, NiPc-MOF was grown in situ on nickel foam (NF) via the anodic electrodeposition (AED) approach (abbreviated as NiPc-MOF_{AED} or NiPc-MOF_{AED}@NF). As far as we know, the AED approach has never been used for the synthesis of 2D conductive MOFs. Remarkably, the as-prepared NiPc-MOF_{AED}@NF can be

directly utilized as electrodes for flexible supercapacitors, which has also been well explored in this paper.

2. Results and discussion

Fig. 1 shows the chemical structure of NiPc-NH₂ (precursor) and NiPc-MOF. Herein, NiPc-MOF was prepared in a two-electrode setup through the AED approach. NF was employed as the anodic electrode. To probe the electrochemical growth of NiPc-MOF_{AED}@NF, the whole process was monitored using scanning electron microscopy (SEM). The mechanism of NiPc-MOF deposition is illustrated in Fig. 2. During the electrodeposition process, NF gradually dissolved under positive potential, releasing nickel ions (Ni²⁺) into the electrolyte solution (Fig. 2a). When the concentration of Ni²⁺ reached critical condition, coordination reaction between Ni2+ and NiPc-NH2 was evoked, producing Ni(isq)2 linkers (bis(o-diiminobenzosemiquinonate) nickel(II)) between NiPc ligands [26]. As a result, 2D planar nanosheets with four-fold symmetry within the ab planes were deposited on the surface of NF. At the beginning stage, isolated NiPc-MOF particles were observed over NF (Fig. 2b). Then, at next stage, many new NiPc-MOF particles appeared, which tended to pack on top or next to those existing particles, forming MOF islands on the NF (Fig. 2c). As time passed, amounts of NiPc-MOF particles were grown onto NF and eventually almost all the exposed NF surfaces were covered with NiPc-MOF particles (Fig. 2d). With more and more NiPc-MOF particles growing, the color of the NF gradually changed from silvery gray to totally black (Fig. S1). Notably, the growth rate and loading amounts of NiPc-MOF particles can be controlled by adjusting the electrolytic voltage (current), deposition time, and electrode area, as well as the precursor concentration, pH value, and reaction temperature. To simplify the discussion, all NiPc-MOFAED@NF samples in this report were synthesized at identical conditions (except for deposition time) unless otherwise stated.

To gain insight into mechanism of nucleation, the nucleation pathway was analyzed using theoretical simulations, which predict that NiPc-MOF_{AED} nucleates exclusively in the interfacial region 1.0–1.5 nm from the surfaces of the NF electrode (Fig. 2e). Classical density functional theory (cDFT) simulations predict that under electrochemical synthesis conditions used in this study Ni $^{2+}$ ions and NiPc-NH precursor molecules are driven toward the interface by ion correlation forces and accumulate 1.0 nm and 1.5 nm from the NF surface, respectively. The large energy barriers at the electrode surface prevents Ni $^{2+}$ and precursor deposition onto NF surface creating ideal conditions for their coordination in the solvent-separated state. Because NiPc-MOF_AED nucleation takes place in the narrow region in the vicinity of the electrode and not directly on the NF surface, a uniform particle size and uniform coverage is predicted.

As is apparently revealed in the SEM image (Fig. 3a), the as-prepared $NiPc\text{-}MOF_{AED}$ presents stacked submicron sphere-like morphologies. To confirm the successful synthesis of the MOF structure, NiPc-MOF_{AED} was collected from NF through sonication. For comparison, NiPc-MOF synthesized with the solvothermal approach (NiPc-MOF_{Sol}) was also prepared following our previously reported procedure. Fourier transform infrared (FT-IR) spectra reveal the disappearance of the N-H signals (Fig. S2) in NiPc-MOFAED [27], indicating the complete coordination of NiPc-NH₂ with Ni²⁺. Further powder X-ray diffraction (XRD) measurements demonstrate their long-range orderly arrangement (Fig. 3b). The locations of reflection peaks in NiPc-MOFAED are in good agreement with those of NiPc-MOF_{Sol}, indicating that the AED approach did not change its crystallographic symmetry. The excellent long-range order of NiPc-MOF_{AED} is also confirmed by high-resolution (HR) transmission electron microscopy (TEM) images (Fig. 3c-d), which show a direct view of the square unit cells at the molecular level with a cell parameter of \sim 1.7 nm. Furthermore, we recorded the high angle annular dark field (HAADF)-TEM image of NiPc-MOFAED (Fig. 3e) in the same area with Fig. 3d, which shows a uniform distribution of C, N, O, and Ni throughout the sample (Fig. 3f). Moreover, X-ray photoelectron

spectroscopy (XPS) spectra combined with energy dispersive X-ray spectroscopy were also collected for NiPc-MOF_{AED} (Fig. S3 and Fig. S4). Both spectra show the existence of C, N, Ni, and O elements. When compared with the XPS spectra of NiPc-MOF_{Sol}, no significant difference was observed in both the survey scan and the fine spectra of Ni and N elements, suggesting their identical chemical composition. The porosity of NiPc-MOF_{AED} was analyzed by N₂ adsorption isotherms, which show a high Brunauer-Emmett-Teller (BET) surface area of $\sim\!343~\text{m}^2~\text{g}^{-1}$ (Fig. S5). All these results indicate that 2D conductive NiPc material could be synthesized and loaded successfully via the AED approach on the NF substrate directly, which is a promising material for supercapacitors owing to the high surface area and intrinsic nature of decent conductivity.

The as-prepared NiPc-MOF_{AED}@NF was then directly fabricated into symmetric flexible supercapacitors (Fig. S6a). Owing to high ionic conductivity [28] and beter symmetry during cyclic voltammetry process (compared with PVA/LiCl, Fig. S6b), PVA/LiClO₄ gel was utilized as aqueous electrolyte. For comparison, NiPc-MOF powder was also loaded onto NF through the traditional pressing process (NiPc-MOF_{press}@NF) and the slurry coating method (NiPc-MOF_{dropcast}@NF), respectively, and was further fabricated into flexible supercapacitors. We also tried the direct growth of NiPc-MOF on NF through solvothermal approach (NiPc-MOF_{S0l}@NF), which was then fabricated into supercapacitors. To rule out the influence of NF or other nickel species during electrode-position, blank NF was also electrolyzed following an identical AED process (without adding NiPc-NH₂ precursor) before it was fabricated into supercapacitors (electrolyzed blank NF). The detailed fabrication process is provided in experimental details.

The supercapacitor performance of the device was initially evaluated through cyclic voltammetry (CV) measurements (Fig. S7). Obviously, NiPc-MOFAED@NF presents the highest capacitance, which shows an enormous advantage (>10-fold) over NiPc-MOF_{Sol}@NF, NiPc-MOFpress@NF, and NiPc-MOF_{dropcast}@NF. The significantly enhanced capacitance of NiPc-MOFAED@NF is mainly due to the novel electrode fabrication approach. When we tried the direct growth of NiPc-MOF on NF through solvothermal approach, most of the MOF particles were formed in solution instead of depositing on NF, leaving NiPc-MOF-Sol@NF with poor MOF loading. Moreover, in the traditional solvothermal synthesis process, MOF sheets tend to aggregate with each other owing to their strong π - π interaction, which is very difficult to exfoliate even with vigorous sonication. So when loaded onto NF through the pressing process or slurry coating method, these MOF powders tend to exist as packed particles dispersed over NF with low coverage (Fig. S8). Thus, most sites in NiPc-MOF powder are not accessible for charge storage in NiPc-MOFpress@NF, NiPcMOF_{dropcast}@NF, and NiPc-MOF_{Sol}@NF. In contrast, with the AED method, most MOF particles were formed on NF rather than in solution. In addition, NiPc-MOF was uniformly deposited onto NF, and the aggregation of MOF sheets was effectively suppressed, leaving thin film of NiPc-MOF_{AED}@NF with more active sites for charge storage in NiPc-MOF_{AED}@NF even at a low loading amount. Notably, the integral area of the CV curve for electrolyzed blank NF is almost negligible, suggesting that NF has almost no contribution to the capacitance.

When examined with different scan rates (2 mV s⁻¹-50 mV s⁻¹), all CV profiles for NiPc-MOF_{AED}@NF show nearly rectangular shape without redox activity, indicating the decent capacitive charge storage mechanism of NiPc-MOF_{AED}@NF electrode (Fig. 4a). For CV curves, the total stored charge can be divided into surface-limited contribution and diffusion-limited contribution using Dunn's method [29]. The calculation process has been provided in experimental details. As shown in Fig. S9c, the surface-limited process contributes around 81.1% of the total charge storage at a scan rate of 20 mV s⁻¹. The contribution of surface-limited process at different scan rates were also calculated (54.4% at 2 mV s⁻¹, 65.5% at 5 mV s⁻¹, 76.0% at 10 mV s⁻¹, and 91.7% at 50 mV s⁻¹), which further demonstrate the dominance of the surface-limited process to overall charge storage.

Galvanostatic charge-discharge (GCD) experiments were then carried out at various current densities (0.04 mA cm⁻²-0.4 mA cm⁻²) to further characterize supercapacitor performance (Fig. 4b). At the low current density of 0.04 mA cm⁻², triangular trace was recorded, corresponding to the double layer capacitive character. As the discharge rate increased to 0.4 mA cm⁻², the triangular shape was still maintained, suggesting that NiPc-MOFAED@NF possesses good rate capability. The calculated coulombic efficiency increased from 84.7% to 87.0% along with the increase of the current density from 0.04 to 0.4 mA cm $^{-2}$. Significantly, due to the existence of equivalent series resistance (ESR), a sudden potential drop always occurred at the beginning of a constant current discharge. Based on the value of voltage drop and discharge current, the ESR for the fully assembled supercapacitor made from NiPc-MOF_{AED}@NF was calculated to be \sim 50 Ω (Fig. S10). To further disclose the different parts of ESR, we also performed electrochemical impedance spectroscopy (EIS) measurements in the frequency range from 100 kHz to 0.01 Hz (Fig. S11). In the Nyquist plots, three segments (the small semicircle, the Waburg diffusion line, and the capacitive line) are clearly visible. Particularly, the linear curve in the low-frequency region represents typical supercapacitor characteristics. The ohmic resistance and the charge transfer resistance were estimated to be $\sim 1.5 \Omega$ and $\sim 36 \Omega$, respectively, which is consistent with ESR data. Compared with other interdigital supercapacitors [30], the resistance of the NiPc-MO-FAED@NF supercapacitor is pretty small, which guarantees its high

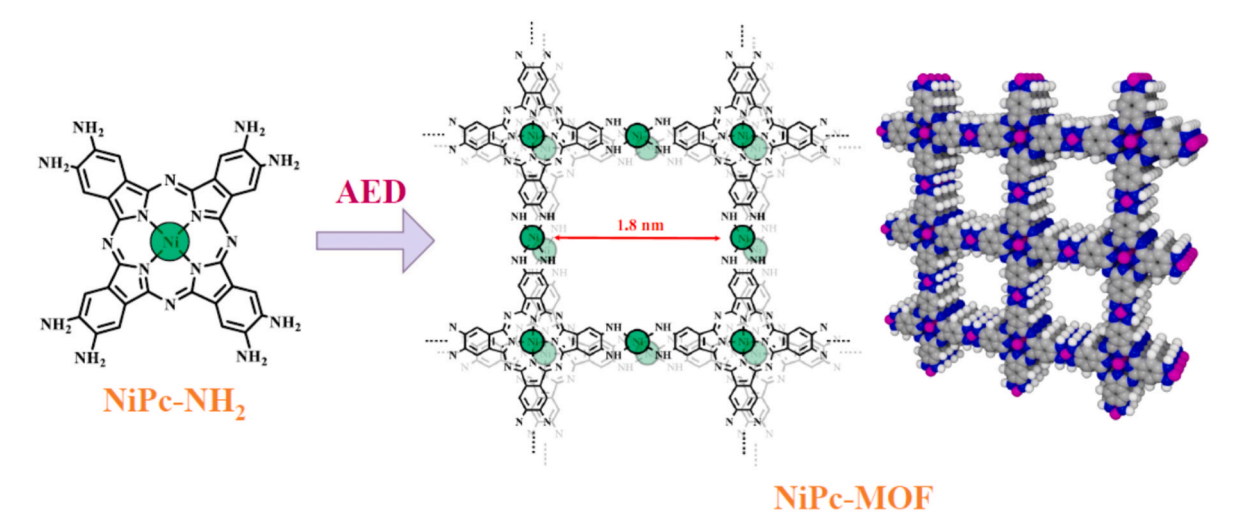


Fig. 1. Chemical structure of NiPc-NH₂ (precursor) and NiPc-MOF.

capacitance performance. We also conducted EIS measurements for NiPc-MOF $_{press}$ @NF and NiPc-MOF $_{dropcast}$ @NF-based supercapacitors. Because of the low coverage of MOF powder, their Nyquist plots demonstrate smaller resistance. Even so, their charge storage performance are really poor.

The specific areal capacitances of NiPc-MOFAED@NF supercapacitor was then calculated from galvanostatic discharge curves at various current densities. (Fig. 4c). At the low current density of 0.04 mA cm⁻². the areal capacitance of the NiPc-MOF $_{\!AED}@$ NF supercapacitor is as high as 11.5 mF cm⁻², which outperforms a majority of pristine MOF-based and conducting polymer-based supercapacitors, such as nZIF-8 (0.268 mF cm⁻²) [12], nNi-MOF-74 (0.415 mF cm⁻²) [12], and benzene-bridged polypyrrole (PbPPy, 0.35 and 0.95 mF cm⁻²) [21]. This result is even superior to some graphene/carbon nanotube (CNT) containing supercapacitors, such as graphene-CNT (G-CNT, 2.16 and 3.93 mF cm⁻²) [31], water-dispersible graphene/sulfonated polyaniline (rG/SP, 3.13 mF cm⁻²) [32], and reduced multilayer graphene oxide (RMGO, 3.13 mF cm^{-2}) [33]. When the current density increased to 0.4 mA cm⁻², its areal capacitance is still as high as 8.1 mF cm⁻², indicating that the NiPc-MOF_{AFD}@NF supercapacitor possess high rate performance. Moreover, according to the mass loading amount of NiPc--MOF_{AFD}, the specific gravimetric capacitance for NiPc-MOF_{AFD}@NF electrode versus current densities was also plotted and is presented in Fig. 4c. At low current density of 0.04 mA cm⁻², the NiPc-MOF_{AED}@NF electrode delivered a gravimetric capacitance of 120 F g⁻¹. This value also surpasses most reported values of pristine MOF (including conductive MOF)-based materials, such as ZIF-67 (0.133 F g^{-1}) [34], $Ni_3(HITP)_2$ (111 F g⁻¹) [9], and Cu-CAT (35 F g⁻¹) [22]. The NiPc--MOF_{AED}@NF supercapacitor also exhibited remarkable cycling stability. About 77.5% of the initial capacitance was still maintained after 10000 GCD cycles (Fig. 4d and Fig. S12).

On the other hand, flexibility is another important metric for portable and miniature devices. To illustrate the flexible properties of the NiPc-MOF_{AED}@NF supercapacitor, we tested its CV curves at different bending angles (Fig. 4e and Fig. S13), which are well overlapped without a significant shape change, demonstrating its excellent mechanical flexibility. In addition, NiPc-MOF_{AED}@NF supercapacitor was bent at 90° for 2000 times and the corresponding CV curves were also characterized as shown in Fig. S14. No significant changes were recorded after bending 2000 times, manifesting excellent bending stability of NiPc-MOF_{AED}@NF supercapacitor. In order to intuitively manifest the high performance, the NiPc-MOF_{AED}@NF supercapacitor was also tested to drive commercial light-emitting diodes (LEDs). It can be seen that a red LED (\sim 2.0 V) was successfully lighted by three seriesconnected devices (Fig. 4f), highlighting the prospective future of the NiPc-MOF_{AED}@NF supercapacitor.

To investigate the chemical stability of NiPc-MOF $_{AED}$, we collected samples from NF after long-term cycling stability measurements and samples from NF after bending 2000 times. The SEM images and XPS spectra (Fig. S15 and Fig. S16) does not show a significant difference before and after cycling measurements and bending measurements, indicating its robust chemical stability.

All these above results suggest that the NiPc-MOF_{AED}@NF supercapacitor possesses outstanding charge storage performance and robust stability. Neverthless, its voltage window was limited to 0.8 V since aqueous electrolyte (PVA/LiClO₄) was utilized. To overcome this drawback, we have explored the NiPc-MOF_{AED}@NF capacitor performance in organic electrolyte. Thanks to the large voltage window and suitable ionic diameters for the channels in NiPc-MOF, 1 M TEABF₄/ Acetonitrile was selected as electrolyte [9]. To our surprise, when

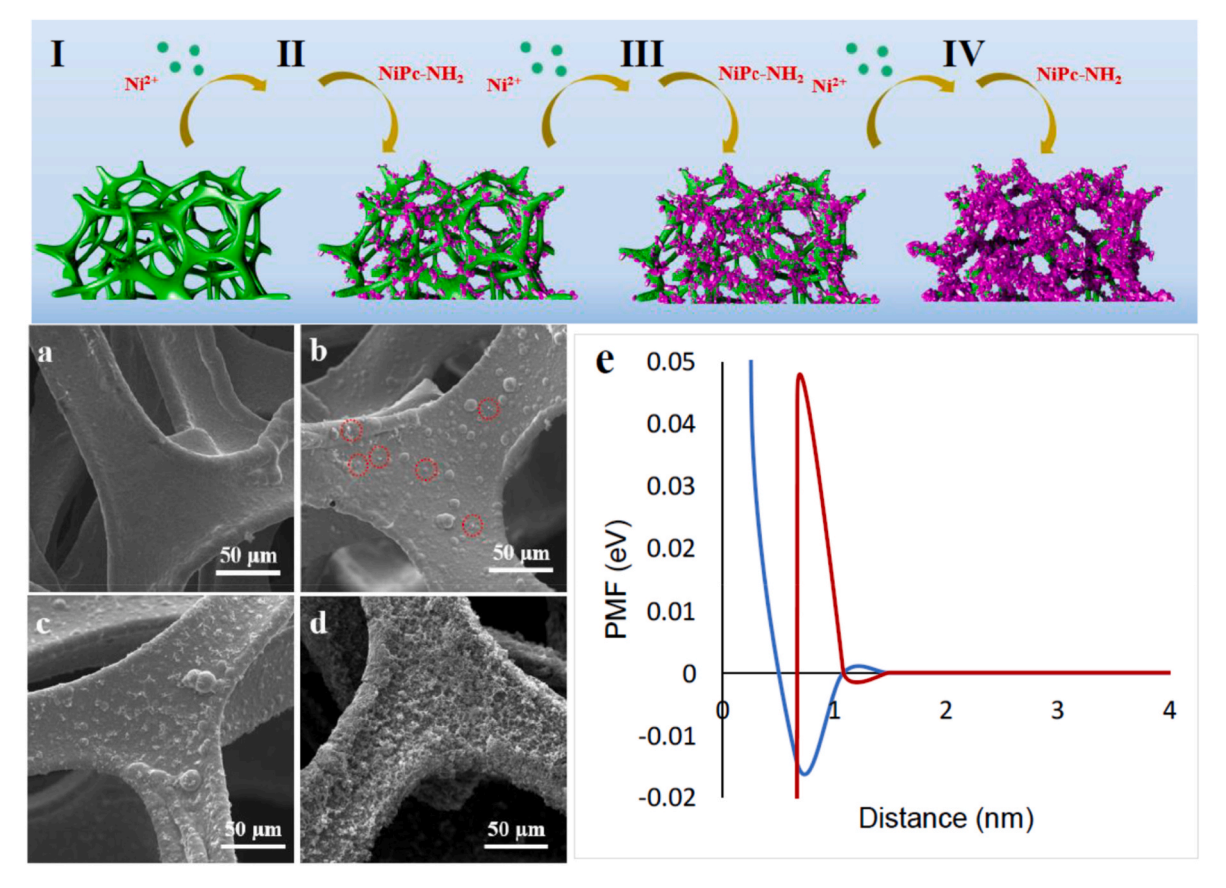


Fig. 2. Proposed *in situ* electrodeposition mechanism of NiPc-MOF_{AED}@NF (top, I-IV) and corresponding SEM images of NiPc-MOF_{AED}@NF after different deposition times (bottom): (a) 0 h (blank NF); (b) 0.5 h; (c) 2 h; (d) 8 h. (e) Nucleation mechanism of NiPc-MOF_{AED}. Simulated potential of mean force of Ni²⁺ (blue line) and NiPc-NH⁻ (red line) at NF electrode. (For interpretation of the references to color in this figure legend, the reader is referred to the Web version of this article.)

fabricated in an organic system, the NiPc-MOF_{AFD}@NF supercapacitor (Fig. S17) shows a great advantage over the aqueous system. First of all, the voltage window is greatly extended from 0.8 V to 2.7 V. Meanwhile, all CV profiles at different scan rates (5 mV s⁻¹-100 mV s⁻¹) display a rectangular shape (Fig. 5a). The calculated contribution of surface-limited process at different scan rates (Fig. S18c, 60.8% at 5 mV s^{-1} , 66.3% at 10 mV s^{-1} , 77.8% at 20 mV s^{-1} , 85.8% at 50 mV s^{-1} , and 93.1% at 100 mV s⁻¹) suggest that the surface-limited process dominates total charge storage. All GCD curves at different current density (0.1 mA cm⁻²-1 mA cm⁻²) maintain a decent triangular shape (Fig. 5b). The corresponding coulombic efficiency for organic systems were also determined (increased from 86.3% at 0.1 mA cm⁻² to 92.7% at 1 mA cm⁻²). Notably, a very high areal capacitance of 22.1 mF cm⁻² was recorded at a current density of 0.1 mA cm⁻² (Fig. 5c), which is almost twice that of the aqueous system. The corresponding specific gravimetric capacitance was calculated to be as high as 230 F g⁻¹, which is even superior to or comparable with many activated carbons-doped complexes including GO-doped carbon (190 F g⁻¹) [35], 3D-graphene (186 F g⁻¹) [36], and some battery-type MOF-based supercapacitors including Ni-MOF/PANI/NF (113.6 F g⁻¹) [37], Ni-CAT (320 F g⁻¹) [38]. Moreover, in the organic system, the NiPc-MOF_{AFD}@NF supercapacitor exhibited excellent cycling stability, with over 90% of capacitance retention even after more than 10,000 charge-discharge cycles (Fig. 5d and Fig. S22). As for flexibility, similar to its behavior in the aqueous system, no significant change in CV curves has been observed at different bending angles ranging from 0° to 90° (Fig. 5e and Fig. S23). Owing to the large voltage window, in an organic system, one NiPc-MOFAED@NF supercapacitor is adequate to light a green LED (~2.4 V) as shown in Fig. 5f. Therefore, NiPc-MOF_{AED}@NF has exhibited impressive capacitor performance not only in the aqueous system, but also in the organic system (more data for the organic system are provided in Supporting Information, Figs. S17-S23). To gain insight into the enhanced capacitor performance of NiPc-MOFAED@NF supercapacitor in the organic system, we conducted static contact angle measurements. As shown in Fig. S24, the contact angle of water on the NiPc-MOF_{AED} film was measured to be $\sim\!40^\circ$. In sharp contrast, the angle of acetonitrile on the NiPc-MOF_{AED} film was significantly decreased to $\sim\!27.5^\circ$, suggesting that NiPc-MOF_{AED} possesses better wettability in acetonitrile than water, which will facilitate charge transfer and boost charge storage.

To further explore the areal power density and areal energy density of the NiPc-MOF_AED@NF supercapacitor, Ragone plots of samples are depicted in Fig. 6. In the aqueous system, the NiPc-MOF_AED@NF supercapacitor delivered an areal power density of 160 $\mu W~cm^{-2}$ at a high discharge rate of 0.4 mA cm $^{-2}$ and an areal energy density of 1.03 $\mu Wh~cm^{-1}$ at a low discharge rate of 0.04 mA cm $^{-2}$, while in the organic system, these values are significantly increased to 1.35 mW cm $^{-2}$ of areal power density at a high discharge rate of 1 mA cm $^{-2}$ and 22.4 $\mu Wh~cm^{-1}$ of areal energy density at a low discharge rate of 0.1 mA cm $^{-2}$. According to these results, the NiPc-MOF_AED@NF supercapacitor is superior to many reported supercapacitors, some of which are also included in Fig. 6 [30,32,33,39–42].

3. Conclusions

In summary, we have demonstrated that the electrochemical deposition technique is a promising approach to fabricating a pristine 2D conductive MOF-based high-performance supercapacitor. Through the *in situ* AED approach, the NiPc-MOF was uniformly deposited onto NF substrates (NiPc-MOF_{AED}@NF), which could be directly used as electrodes of supercapacitors. The simplified electrode fabrication process, that does not involve binders and conductive additives, would significantly reduce the cost and will have enormous potential for the applications of NiPc-MOF in energy storage. The outstanding performance of the NiPc-MOF_{AED}@NF supercapacitor, including high specific areal capacitances (11.5 mF cm $^{-2}$ in aqueous electrolyte and 22.1 mF cm $^{-2}$ in organic electrolyte), preeminent areal power density (1.35 mW cm $^{-2}$ at 1 mA cm $^{-2}$, organic system) and energy density (22.4 μ Wh cm $^{-1}$ at 0.1

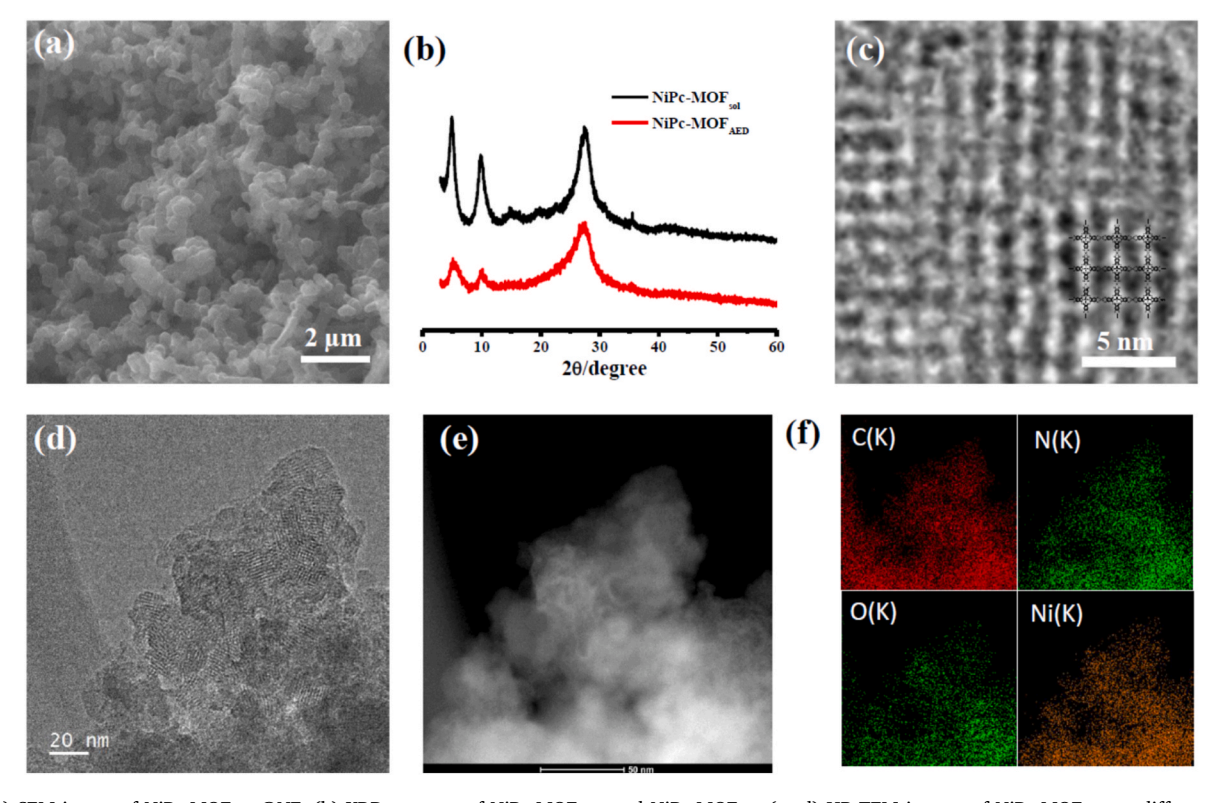


Fig. 3. (a) SEM image of NiPc-MOF_{AED}@NF. (b) XRD patterns of NiPc-MOF_{AED} and NiPc-MOF_{Sol}. (c-d) HR-TEM images of NiPc-MOF_{AED} at different scales. (e) HAADF-TEM image of NiPc-MOF_{AED} in the same area in 3d. (f) Elemental mapping show homogenous distribution of C, N, O, and Ni.

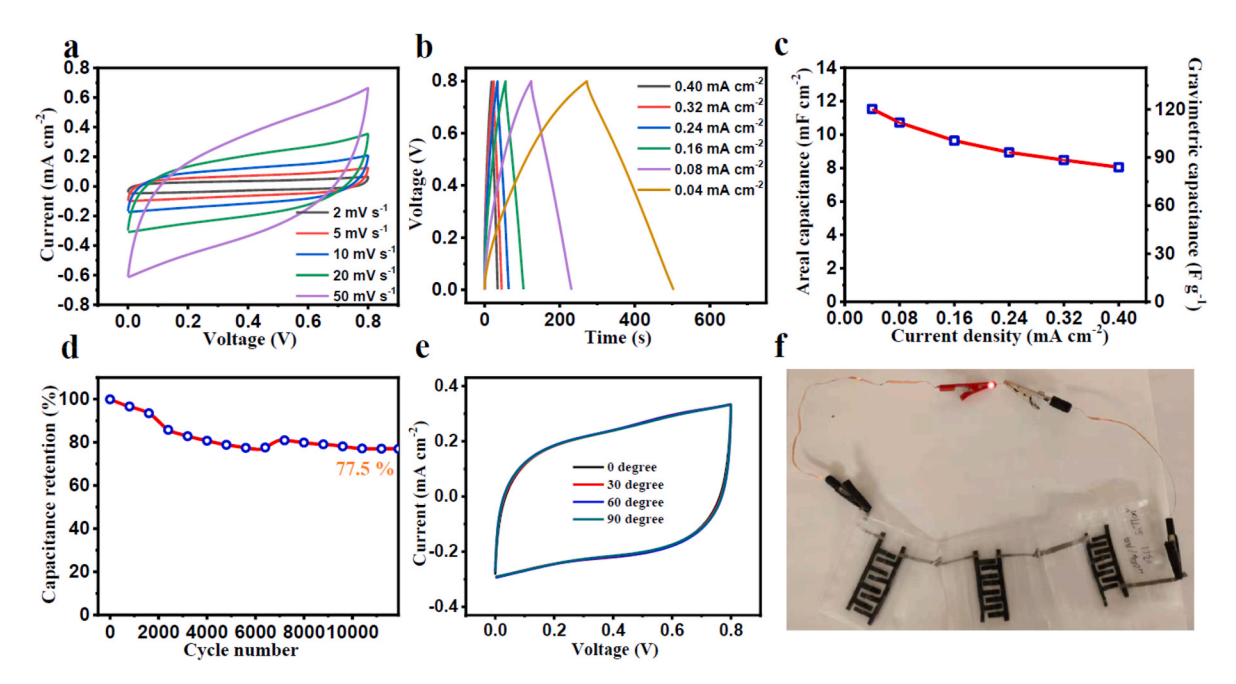


Fig. 4. NiPc-MOF_{AED}@NF-based supercapacitor in aqueous system (PVA/LiClO₄). (a) CV curves at various scan rates of 2–50 mV s⁻¹. (b) GCD curves at various current densities of 0.04–0.4 mA cm⁻². (c) Specific areal capacitances and corresponding specific gravimetric capacitance of each electrode calculated from GCD curves under various current density. (d) Capacitance retention under repeated cycling for more than 10000 cycles. (e) CV curves of supercapacitor at bending angles of 0°, 30°, 60°, and 90°. Scan rate: 20 mV s⁻¹. (f) Photograph of a red LED powered by the three series-connected supercapacitors. (For interpretation of the references to color in this figure legend, the reader is referred to the Web version of this article.)

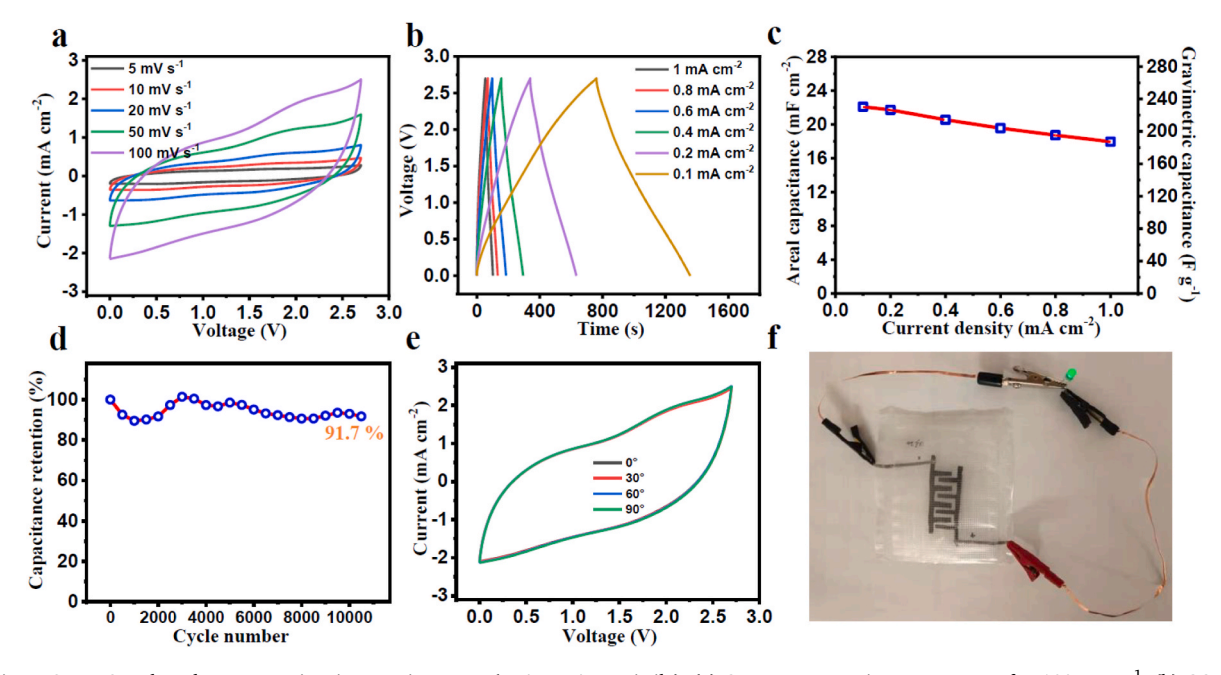


Fig. 5. NiPc-MOF_{AED}@NF-based supercapacitor in organic system (TEABF₄/Acetonitrile). (a) CV curves at various scan rates of 5–100 mV s⁻¹. (b) GCD curves at various current densities of 0.1–1 mA cm⁻². (c) Specific areal capacitances and corresponding specific gravimetric capacitance of supercapacitor calculated from GCD curves under various current densities. (d) Capacitance retention under repeated cycling for more than 10,000 cycles. (e) CV curves of supercapacitor at bending angles of 0° , 30° , 60° , and 90° . Scan rate: 100 mV s⁻¹. (f) Photograph of a green LED powered by one supercapacitor. (For interpretation of the references to color in this figure legend, the reader is referred to the Web version of this article.)

mA cm⁻², organic system), robust cycling stability as well as prominent mechanical flexibility, were further disclosed by electrochemical measurements. This present study not only report an advanced phthalocyanine-based MOF material for a high-performance supercapacitor, but also opens up a novel avenue for the *in situ* growth of the 2D conductive MOF. Further challenges, including the *in situ*

electrodeposition of other metal-based conductive MOFs on different substrates and their applications in other field (including but not limited to catalysis, sensors, and batteries) are subjects of ongoing research in our laboratory.

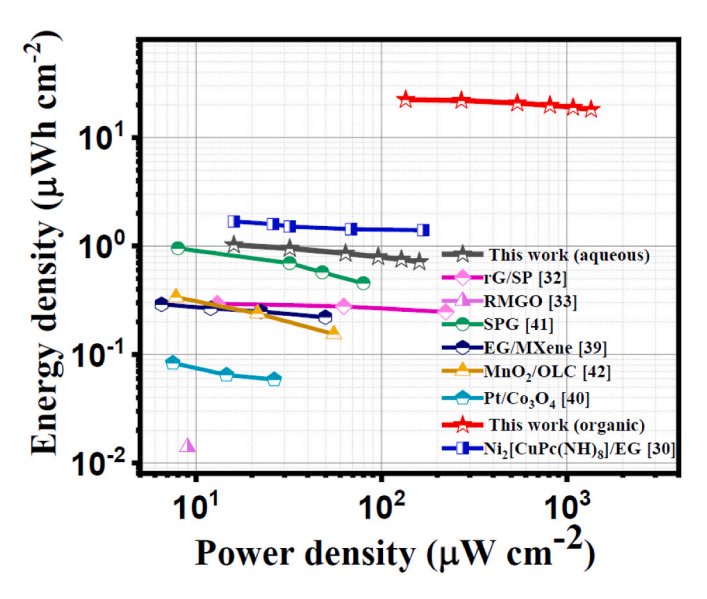


Fig. 6. Ragone plots for NiPc-MOF $_{AED}$ @NF-based supercapacitor in both aqueous and organic electrolyte. For comparison, Ragone plots of many reported supercapacitors based on various active materials are also depicted.

4. Experimental details

4.1. Synthesis of NiPc-NH2 and NiPc-MOFSol

NiPc-NH₂ (precursor) and NiPc-MOF_{Sol} was synthesized according to our previously reported method [25].

4.2. Anodic electrodeposition of NiPc-MOF@NF

The electrodepositions were conducted in a small (10 mL) two-electrode set-up using NF as the working electrodes and a nickel foil as the counter electrode. Due to the poor solubility of NiPc-NH $_2$ in water, DMF (4 mL) was utilized as solvent, while 1-Butyl-3-methylimidazolium chloride (0.1 M) was used as electrolyte. The concentration of NiPc-NH $_2$ was set to (7.2 \times 10 $^{-4}$ M, 2 mg/4 mL). To facilitate electrodeposition, 0.05 mL concentrated aqueous ammonia was added. During electrodeposition, the dark red solution gradually changed into colorless, meanwhile black MOF particles were grown on NF electrode. All the electrodepositions were performed under same potential (1.1 V) but different durations.

4.3. Preparation of electrolyte

4.3.1. PVA/LiClO₄ gel preparation

A total of 0.75 g PVA (molecular weight 86,000) and 2.1 g LiClO₄ were added into 7.5 mL of deionized water, then the mixture was stirred at 95 °C until all the solids were completely dissolved. The forming clear solution is PVA/LiClO₄ gel, which serves as an aqueous electrolyte for supercapacitor.

4.3.2. Organic electrolyte preparation

A total of 2.17 g tetraethylammonium tetrafluoroborate (TEABF $_4$) was added to 10 mL of anhydrous acetonitrile (1 M), then the mixture was stirred at room temperature until all the solids were completely dissolved. To avoid the influence of moisture and other active molecules in air, this organic electrolyte was prepared, kept, and used in a glove box (N $_2$ or Ar atmosphere).

4.4. Flexible supercapacitor fabrication

NF was cut into interdigitated electrodes containing 4 fingers. Their apparent areas were estimated according to their weights. Before used, these electrodes were thoroughly cleaned by sonication in 3 M HCl, deionized water, EtOH, and acetone sequentially.

NiPc-MOF_{AED}@NF: Interdigitated NF electrodes were electrodeposited with NiPc-MOF following above process. During electrodeposition, these electrodes were totally immersed into electrolyte solution. The electrodeposition time was set to 8 h to ensure a similar loading amount, which was precisely calculated through ICP-AES. When deposition was completed, these electrodes were gently washed and dried at 60 °C for 2 h. These as-prepared NiPc-MOF_{AED}@NF electrodes were fixed into heat-seal bag in interdigital pattern. Then, 1 mL of electrolyte was filled in these interdigital electrodes (when organic electrolyte is utilized, the fabrication should be conducted in glove box). After being sealed with a household vacuum sealer machine, the flexible supercapacitor was finally fabricated.

<code>NiPc-MOFsol@NF:</code> To realize the direct growth of NiPc-MOF through solvothermal approach, interdigitated NF electrodes were placed in the reaction vessel before synthesis. Then NiPc-NH $_2$ (6 mg, 8.7 μ mol), NiCl $_2$ ·6H $_2$ O (6 mg, 25.3 μ mol), 0.2 mL concentrated aqueous ammonia, and 12 mL DMSO were added into this vessel. The reaction was kept at 60 °C overnight. This procedure were repeated for three times. Then these electrodes were gently washed and dried at 60 °C for 2 h. Thereafter, these electrodes were fabricated into a device following same procedure with NiPc-MOF $_{\Lambda ED}$ @NF.

NiPc-MOF_{press}@**NF**: NiPc-MOF powder was directly pressed into interdigitated NF electrodes at a pressure of 1000 MPa without adding additives. Then these electrodes were fabricated into a device following same procedure with NiPc-MOF_{AED}@NF.

NiPc-MOF_{dropcast}@NF: Initially, the NiPc-MOF ink was prepared by sonicating 2 mg of NiPc-MOF powders in a mixture solution of 1800 μL of ethanol and 200 μL of 5 wt % Nafion solution. Then this ink was carefully dropcast onto interdigitated NF electrodes and dried in vacuum oven. Thereafter, these electrodes were fabricated into a device following same procedure with NiPc-MOF_AED@NF.

Blank NF: The washed interdigitated blank NF electrodes were directly fabricated into a device following same procedure with NiPc-MOF_{AED}@NF.

Electrolyzed blank NF: Interdigitated NF electrodes were electrolyzed following the identical process of NiPc-MOF $_{\rm AED}$ @NF (without adding NiPc-NH $_2$ precursor). Then these electrodes were fabricated into a device following same procedure with NiPc-MOF $_{\rm AED}$ @NF.

4.5. Characterization methods

The as-prepared samples were characterized by X-ray power diffraction (XRD) on a Rigaku D/Max-2500/PC powder diffractometer. Each sample powder was scanned using Cu-Kα radiation with an operating voltage of 40 kV and a current of 200 mA. The scan rate of 5°/min was applied to record the XRD patterns in the range of 3-60° at a step size of 0.02°. The morphologies were examined by scanning electron microscopy (SEM, Quanta 200 FEG, FEI) and transmission electron microscopy (TEM, Titan 80-300, FEI) operated at 300 kV. A high-angle annular dark field (HAADF) detector was used in the STEM mode, with the inner detection angle three times higher than the probe convergence angle. Compositional analysis was performed with energy-dispersive Xray spectroscopy (EDS), using an Oxford X-Max^N 100TLE silicon drift detector. The EDS data collection and processing was performed with Oxford's Aztec software package. X-ray photoelectron spectroscopy (XPS) measurements were carried out on a VG ESCALAB MK2 spectrometer with monochromatized Al-K α excitation. Fourier transform infrared (FT-IR) spectroscopy measurements were carried out on a Thermo Fisher Scientific instrument (Nicolet iS10). Nitrogen adsorption and desorption measurements were performed on a Quantachrome instrument (ASIQM0000-5) and the Brunauer-Emmett-Teller (BET) method was applied to calculate the specific surface areas. Elemental analyses of Ni were conducted on an Optima 7300 DV inductively coupled plasma-atomic emission spectrometry (ICP-AES) instrument.

4.6. Electrochemistry

All the electrochemical experiments were conducted at room temperature on an electrochemical workstation (CHI760E, Shanghai Chen Hua Instrument Co., Ltd.).

The current response at fixed potential in CV curves can be expressed as sum of two components: diffusion-limited process ($av^{1/2}$) and surface-limited process (bv):

$$I = av^{1/2} + bv$$

where I is the measured current, ν is scan rate. a and b are scan rate independent constants which can be determined by plotting $I/\nu^{1/2}$ vs. $\nu^{1/2}$.

The coulombic efficiency $(\boldsymbol{\eta})$ was evaluated from the following equation:

$$\eta = \frac{t_d}{t_c} \times 100\%$$

where t_d is discharging time, t_c is charging time. The equivalent series resistance (*ESR*) was calculated by the following equation:

$$ESR = \frac{V_{drop}}{2I}$$

where V_{drop} is the voltage drop at the beginning of the discharge curve, and I is the discharge current. The specific areal capacitances (C_a) were calculated by the following equation:

$$C_a = \frac{I \times t}{S \times V}$$

where t is the discharge time, S is total area for both electrodes, and V is discharge voltage. The specific gravimetric capacitances for electrode (C_g) were calculated by the following equation:

$$C_g = \frac{4I \times t}{m \times V}$$

where m is total loading mass for both electrodes. The areal energy density (E_a) was calculated by the following equation:

$$E_a = \frac{C_a \times V^2}{2 \times 3600}$$

The areal power density (P_a) was calculated by the following equation:

$$P_a = \frac{E_a \times 3600}{t}$$

CRediT authorship contribution statement

Hongxing Jia: Conceptualization, Methodology, Writing – original draft. Shun Lu: Formal analysis, Data curation, Figure draw, Writing – review & editing. Sun Hae Ra Shin: Investigation, Formal analysis, Characterization. Maria L. Sushko: Software, Formal analysis, Writing – review & editing, Simulation, Characterization. Xiaoping Tao: Investigation, Formal analysis, Writing – review & editing. Matthew Hummel: Data curation, Characterization. Praveen K. Thallapally: Supervision, Writing – review & editing. Jun Liu: Supervision, Writing – review & editing. Zhengrong Gu: Supervision, Project administration, Funding acquisition, Writing – review & editing.

Declaration of competing interest

The authors declare that they have no known competing financial interests or personal relationships that could have appeared to influence the work reported in this paper.

Acknowledgement

This work was supported by NSF EPSCoR (No. OIA-1849206), and NASA EPSCoR (No. NNX16AQ98A). Theoretical simulations, XPS, and TEM characterization were supported by the U.S. Department of Energy, Office of Science, Basic Energy Sciences, Division of Materials Sciences and Engineering, under Award KC020105-FWP12152. PNNL is operated by Battelle for the Department of Energy under contract no. DE-AC05-76RLO1830. We also thank Ailin Guo for helping with FT-IR measurements, Wei He for helping with contact angle measurements, and Haibo Chi for helping with manuscript revision. The authors want to thank South Dakota 2D Materials for Biofilm Engineering, Science and Technology Center (2DBEST) for supporting this project.

Appendix A. Supplementary data

Supplementary data to this article can be found online at https://doi.org/10.1016/j.jpowsour.2022.231163.

References

- [1] B. Li, H.M. Wen, Y.J. Cui, W. Zhou, G.D. Qian, B.L. Chen, Adv. Mater. 28 (2016) 8819–8860.
- [2] E.D. Bloch, W.L. Queen, R. Krishna, J.M. Zadrozny, C.M. Brown, J.R. Long, Science 335 (2012) 1606–1610.
- [3] J.D. Pang, F.L. Jiang, M.Y. Wu, C.P. Liu, K.Z. Su, W.G. Lu, D.Q. Yuan, M.C. Hong, Nat. Commun. 6 (2015) 7575.
- [4] J.C. Yu, Y.J. Cui, H. Xu, Y. Yang, Z.Y. Wang, B.L. Chen, G.D. Qian, Nat. Commun. 4 (2013) 2719.
- [5] X.J. Zhang, V. Vieru, X.W. Feng, J.L. Liu, Z.J. Zhang, B. Na, W. Shi, B.W. Wang, A. K. Powell, L.F. Chibotaru, S. Gao, P. Cheng, J.R. Long, Angew. Chem. Int. Ed. 54 (2015) 9861–9865.
- [6] A.J. Lan, K.H. Li, H.H. Wu, D.H. Olson, T.J. Emge, W. Ki, M.C. Hong, J. Li, Angew. Chem. Int. Ed. 48 (2009) 2334–2338.
- [7] J.S. Seo, D. Whang, H. Lee, S.I. Jun, J. Oh, Y.J. Jeon, K. Kim, Nature 404 (2000) 982–986.
- [8] M.X. Wu, Y.W. Yang, Adv. Mater. 29 (2017) 1606134.
- [9] D. Sheberla, J.C. Bachman, J.S. Elias, C.J. Sun, Y. Shao-Horn, M. Dincă, Nat. Mater. 16 (2017) 220–224.
- [10] X.Y. Chu, F.L. Meng, T. Deng, W. Zhang, Nanoscale 13 (2021) 5570-5593.
- [11] P. Pachfule, D. Shinde, M. Majumder, Q. Xu, Nat. Chem. 8 (2016) 718–724.
- [12] K.M. Choi, H.M. Jeong, J.H. Park, Y.B. Zhang, J.K. Kang, O.M. Yaghi, ACS Nano 8 (2014) 7451–7457.
- [13] L. Wang, X. Feng, L.T. Ren, Q.H. Piao, J.Q. Zhong, Y.B. Wang, H.W. Li, Y.F. Chen, B. Wang, J. Am. Chem. Soc. 137 (2015) 4920–4923.
- [14] X.T. Xu, J. Tang, H.Y. Qian, S.J. Hou, Y. Bando, M.S.A. Hossain, L.K. Pan, Y. Yamauchi, ACS Appl. Mater. Interfaces 9 (2017) 38737–38744.
- [15] T. Kambe, R. Sakamoto, K. Hoshiko, K. Takada, M. Miyachi, J.H. Ryu, S. Sasaki, J. Kim, K. Nakazato, M. Takata, H. Nishihara, J. Am. Chem. Soc. 135 (2013) 2462–2465.
- [16] R.H. Dong, M. Pfeffermann, H.W. Liang, Z.K. Zheng, X. Zhu, J. Zhang, X.L. Feng, Angew. Chem. Int. Ed. 54 (2015) 12058–12063.
- [17] E.M. Miner, T. Fukushima, D. Sheberla, L. Sun, Y. Surendranath, M. Dincă, Nat. Commun. 7 (2016) 10942.
- [18] M.G. Campbell, D. Sheberla, S.F. Liu, T.M. Swager, M. Dincă, Angew. Chem. Int. Ed. 54 (2015) 4349–4352.
- [19] S. Bi, H. Banda, M. Chen, L. Niu, M.Y. Chen, T.Z. Wu, J.S. Wang, R.X. Wang, J. M. Feng, T.Y. Chen, M. Dincă, A.A. Kornyshev, G. Feng, Nat. Mater. 19 (2020) 552–558.
- [20] D.W. Feng, T. Lei, M.R. Lukatskaya, J. Park, Z.H. Huang, M. Lee, L. Shaw, S. C. Chen, A.A. Yakovenko, A. Kulkarni, J.P. Xiao, K. Fredrickson, J.B. Tok, X.D. Zou, Y. Cui, Z.A. Bao, Nat. Energy 3 (2018) 30–36.
- [21] K.Y. Jiang, I.A. Baburin, P. Han, C.Q. Yang, X.B. Fu, Y.F. Yao, J.T. Li, E. Cánovas, G. Seifert, J.S. Chen, M. Bonn, X.L. Feng, X.D. Zhuang, Adv. Funct. Mater. 30 (2020) 1908243.
- [22] W.H. Li, K. Ding, H.R. Tian, M.S. Yao, B. Nath, W.H. Deng, Y.B. Wang, G. Xu, Adv. Funct. Mater. 27 (2017) 1702067.
- [23] L.F. Shen, B. Ding, P. Nie, G.Z. Cao, X.G. Zhang, Adv. Energy Mater. 3 (2013) 1484–1489.
- [24] X. Zhang, K. Wan, P. Subramanian, M. Xu, J. Luo, J. Fransaer, J. Mater. Chem. 8 (2020) 7569–7587.

- [25] H.X. Jia, Y.C. Yao, J.T. Zhao, Y.Y. Gao, Z.L. Luo, P.W. Du, J. Mater. Chem. 6 (2018) 1188–1195.
- [26] D. Sheberla, L. Sun, M.A. Blood-Forsythe, S. Er, C.R. Wade, C.K. Brozek, A. Aspuru-Guzik, M. Dincă, J. Am. Chem. Soc. 136 (2014) 8859–8862.
- [27] F. Yuksel, S. Tuncel, V. Ahsen, J. Porphyr. Phthalocyanines 12 (2008) 123–130.
- [28] N.R. Chodankar, D.P. Dubal, A.C. Lokhande, C.D. Lokhande, J. Colloid Interface Sci. 460 (2015) 370–376.
- [29] T. Brezesinski, J. Wang, S.H. Tolbert, B. Dunn, Nat. Mater. 9 (2010) 146-151.
- [30] M.C. Wang, H.H. Shi, P.P. Zhang, Z.Q. Liao, M. Wang, H.X. Zhong, F. Schwotzer, A. S. Nia, E. Zschech, S.Q. Zhou, S. Kaskel, R.H. Dong, X.L. Feng, Adv. Funct. Mater. 30 (2020) 2002664.
- [31] J. Lin, C.G. Zhang, Z. Yan, Y. Zhu, Z.W. Peng, R.H. Hauge, D. Natelson, J.M. Tour, Nano Lett. 13 (2013) 72–78.
- [32] B. Song, L.Y. Li, Z.Y. Lin, Z.K. Wu, K.S. Moon, C.P. Wong, Nano Energy 16 (2015) 470–478.
- [33] J.J. Yoo, K. Balakrishnan, J.S. Huang, V. Meunier, B.G. Sumpter, A. Srivastava, M. Conway, A.L.M. Reddy, J. Yu, R. Vajtai, P.M. Ajayan, Nano Lett. 11 (2011) 1423–1427.

- [34] Z. Jiang, Z.P. Li, Z.H. Qin, H.Y. Sun, X.L. Jiao, D.R. Chen, Nanoscale 5 (2013) 11770–11775.
- [35] X. Yang, L. Zhang, F. Zhang, T.F. Zhang, Y. Huang, Y.S. Chen, Carbon 72 (2014) 381–386.
- [36] Y. Xu, Z. Lin, X. Huang, Y. Liu, Y. Huang, X. Duan, ACS Nano 7 (2013) 4042–4049.
- [37] Q.H. Cheng, K. Tao, X. Han, Y.J. Yang, Z. Yang, Q.X. Ma, L. Han, Dalton Trans. 48 (2019) 4119–4123.
- [38] Y.L. Li, J.J. Zhou, M.K. Wu, C. Chen, K. Tao, F.Y. Yi, L. Han, Inorg. Chem. 57 (2018) 6202–6205.
- [39] H.Y. Li, Y. Hou, F.X. Wang, M.R. Lohe, X.D. Zhuang, N. Li, X.L. Feng, Adv. Energy Mater. 7 (2017) 1601847.
- [40] X. Ma, S. Feng, L. He, M. Yan, X. Tian, Y. Li, C. Tang, X. Hong, L. Mai, Nanoscale 9 (2017) 11765–11772.
- [41] X.Y. Shi, S.F. Pei, F. Zhou, W.C. Ren, H.-M. Cheng, Z.-S. Wu, X.H. Bao, Energy Environ. Sci. 12 (2019) 1534–1541.
- [42] Y. Wang, Y. Shi, C.X. Zhao, J.I. Wong, X.W. Sun, H.Y. Yang, Nanotechnology 25 (2014), 094010.